Available online at www.sciencedirect.com
ScienceDirect
Engineering Fracture Mechanics 73 (2006) 2829–2848
Engineering Fracture Mechanics
www.elsevier.com/locate/engfracmech

# A bilinear cohesive zone model tailored for fracture of asphalt concrete considering viscoelastic bulk material

Seong Hyeok Song, Glaucio H. Paulino *, William G. Buttlar

*Department of Civil and Environmental Engineering, University of Illinois at Urbana – Champaign, Newmark Laboratory, 205 North Mathews Avenue, Urbana, IL 61801, USA*

Received 1 November 2005; received in revised form 7 April 2006; accepted 11 April 2006
Available online 10 July 2006

**Abstract**

A bilinear cohesive zone model (CZM) is employed in conjunction with a viscoelastic bulk (background) material to investigate fracture behavior of asphalt concrete. An attractive feature of the bilinear CZM is a potential reduction of artificial compliance inherent in the intrinsic CZM. In this study, finite material strength and cohesive fracture energy, which are cohesive parameters, are obtained from laboratory experiments. Finite element implementation of the CZM is accomplished by means of a user-subroutine which is employed in a commercial finite element code (e.g., UEL in ABAQUS). The cohesive parameters are calibrated by simulation of mode I disk-shaped compact tension results. The ability to simulate mixed-mode fracture is demonstrated. The single-edge notched beam test is simulated where cohesive elements are inserted over an area to allow cracks to propagate in any general direction. The predicted mixed-mode crack trajectory is found to be in close agreement with experimental results. Furthermore, various aspects of CZMs and fracture behavior in asphalt concrete are discussed including: compliance, convergence, and energy balance.


*Keywords:* Bilinear cohesive zone model; Fracture; Asphalt concrete; Rate effects; User element (UEL); Compliance; Crack propagation; Convergence

## 1. Introduction

Cohesive zone modeling has gained considerable attention over the past decade, as it represents a powerful yet efficient technique for computational fracture studies. The early conceptual works related to the cohesive zone model (CZM) date back to the early 60s and were carried out by Barenblatt [1,2], who proposed the CZM to study perfectly brittle materials and Dugdale [3], who adopted a fracture process zone concept to investigate ductile materials exhibiting plasticity. During the 90s, leaps were made as a result of the pioneering works by Needleman and his co-workers [4,5], and Camacho and Ortiz [6]. Xu and Needleman [5] proposed a potential-based cohesive zone model in which cohesive elements are inserted into a finite element mesh in

* Corresponding author. Tel.: +1 217 333 3817; fax: +1 217 265 8041.
*E-mail address:* paulino@uiuc.edu (G.H. Paulino).

0013-7944/$ - see front matter © 2006 Elsevier Ltd. All rights reserved.
doi:10.1016/j.engfracmech.2006.04.030

advance, which follow an exponential cohesive law. In such a scheme, as displacement between cohesive elements increases, the traction initially increases, reaches a maximum, and then decays monotonically. On the contrary, Camacho and Ortiz [6] presented a stress-based extrinsic cohesive law where a new surface is adaptively created by duplicating nodes which were previously bonded. Recently, the CZM by Xu and Needleman [5] has been widely used over the model by Camacho and Ortiz [6], because it is relatively easier to implement into the finite element method (FEM). However, the model by Xu and Needleman induces artificial compliance due to the elasticity of the intrinsic cohesive law. To alleviate such problems, Geubelle and Baylor [7] and Espinosa and Zavattieri [8] adopted bilinear cohesive zone models to reduce the compliance by providing an adjustable initial slope in the cohesive law.

A relatively fewer number of modeling studies have been carried out which address fracture in viscoelastic materials. Early works in this area include the important contributions of Knauss [9] and Schapery [10], who developed theories for macroscopic cracks in viscoelastic media. More recently, a number of different attempts have been made to consider rate effects in a material separation model. Knauss and Losi [11] combined a viscoelastic constitutive model with a damage function. Rahulkumar et al. [12] and Allen and Searcy [13] adopted a hereditary integral approach, which is the identical with the formulation for the bulk material, in conjunction with a traction-separation function. Bazant and Li [14] formulated a rate-dependent cohesive crack model. Xu et al. [15] has also proposed a rate-dependent CZM, having both rate-independent and rate-dependent material parameters which are determined from experiments and numerical analysis.

For the study of fracture in asphalt concrete, most efforts to obtain a better understanding of cracking mechanisms in this particulate viscoelastic material have taken an experimental approach [16–19]. Recently, Soares et al. [20] applied a cohesive zone model to investigate mode I crack propagation in the Superpave Indirect Tension Test (IDT) using the cohesive law proposed by Tvergaard [21]. Paulino et al. [22] and Song et al. [23] simulated mode I and mixed-mode crack propagation of laboratory fracture tests, e.g., the single-edge notched beam (SE(B)) test, using a potential based cohesive zone model [5] and investigated various aspects of fracture behavior in conjunction with experiments. Song et al. [24] adopted a bilinear cohesive zone model to effectively reduce the artificial compliance inherent in the intrinsic cohesive law and modeled mixed-mode crack propagation in asphalt concrete. However, the literature is currently devoid of numerical simulations of fracture in asphalt concrete which consider rate effects. Thus, the scope of this study is as follows:

- To numerically quantify the effects of CZM compliance with respect to fracture in asphalt concrete.
- To present a bilinear CZM, which has been implemented as UEL in ABAQUS, to effectively reduce artificial compliance in asphalt concrete fracture simulations.
- To investigate the fracture behavior of asphalt concrete considering bulk (background) material viscoelasticity.
- To simulate mixed-mode crack propagation in a SE(B) test in which cohesive elements with a regular pattern are inserted over an area to allow cracks to grow in any general direction and to minimize influence of mesh discretization on crack trajectory.
- To compare the mixed-mode crack trajectory obtained from CZM simulation with that of experimental results.
- To study numerical convergence in mixed-mode CZM fracture simulation (including influence of finite element discretization).

This paper is organized in the following manner. Section 2 describes the theoretical and numerical aspects of a bilinear CZM, while Section 3 specifically investigates methods to reduce artificial compliance introduced by the intrinsic cohesive zone models in the context of modeling fracture in asphalt concrete. Section 4 introduces basic formulation for viscoelasticity and presents energy balance. Section 5 provides simulation examples of mode I and mixed-mode fracture tests and discusses numerical convergence. Finally, summary and conclusions are presented.

## 2. Theoretical and numerical aspects of a bilinear CZM

In this section, a bilinear cohesive zone model [8] is presented. Then, a numerical implementation of the cohesive law is provided in conjunction with a ABAQUS user element (UEL) subroutine [25].

### 2.1. A bilinear cohesive zone model

Despite the many successful applications of the potential based exponential cohesive law reported in the literature, the model inherently produces artificial compliance due to a pre-peak slope described in this cohesive law. Recently, Espinosa and Zavattieri [8] formulated a bilinear model to reduce CZM compliance by providing an adjustable initial slope in the cohesive law. Fig. 1 shows the bilinear cohesive law in terms of normalized opening tractions and normalized opening displacements for several different ratios of sliding displacements. The pre-peak region represents the elastic part of the intrinsic cohesive law whereas the softening portion after the peak load accounts for various forms of damage occurring in the fracture process zone. Notice that the parameter $\lambda_{cr}$ is non-dimensional displacement in which the traction is a maximum, and is incorporated to reduce the elastic compliance by adjusting the pre-peak slope of the cohesive law. In other words, as the value of $\lambda_{cr}$ decreases, the pre-peak slope of the cohesive law increases and as a result, artificial compliance is reduced.

Non-dimensional effective displacement and effective traction are defined as

$$\lambda_e = \sqrt{\left(\frac{\delta_n}{\delta_c}\right)^2 + \left(\frac{\delta_s}{\delta_c}\right)^2} \quad \text{and} \tag{1}$$

$$t_e = \sqrt{t_n^2 + t_s^2}, \tag{2}$$

respectively; in which subscript e represents effective; $\delta_n$ and $\delta_s$ denote a normal displacement opening and shear sliding, respectively; $\delta_c$ is a critical displacement where complete separation, i.e. zero traction, occurs, and; $t_s$ and $t_n$ are shear and normal tractions, respectively. For $\lambda_e < \lambda_{cr}$, the shear and normal tractions are governed by

$$t_s = \sigma_c \frac{1}{\lambda_{cr}} \left(\frac{\delta_s}{\delta_c}\right) \quad \text{and} \quad t_n = \sigma_c \frac{1}{\lambda_{cr}} \left(\frac{\delta_n}{\delta_c}\right) \tag{3}$$

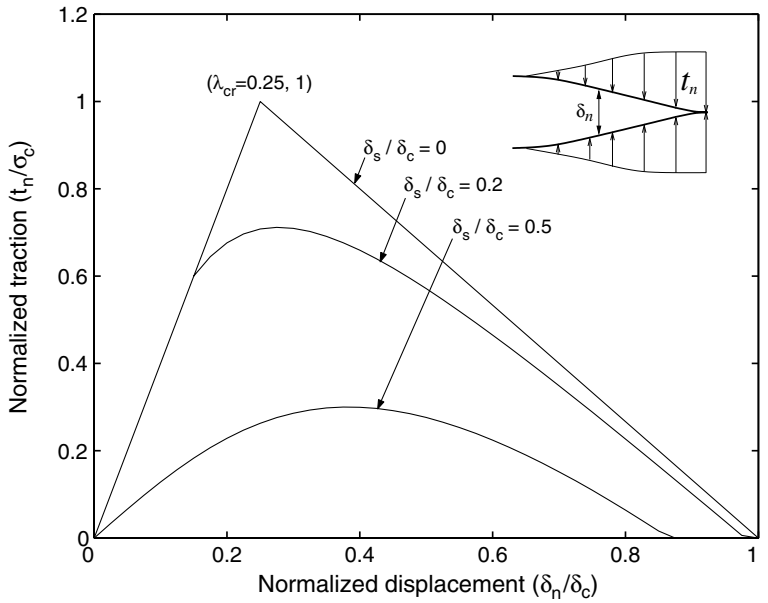


Fig. 1. A cohesive law in terms of normalized opening displacement jump and normalized traction for different ratios of sliding displacements ($\delta_s/\delta_c$). Notice that in mixed-mode, a cohesive law in terms of normalized opening displacement jump and normalized traction is not bilinear; however, in terms of effective quantities, it is always bilinear.

and for $\lambda_e > \lambda_{cr}$, the tractions are described by

$$t_s = \sigma_c \frac{1-\lambda_e}{1-\lambda_{cr}} \frac{1}{\lambda_e}\left(\frac{\delta_s}{\delta_c}\right) \quad \text{and} \quad t_n = \sigma_c \frac{1-\lambda_e}{1-\lambda_{cr}} \frac{1}{\lambda_e}\left(\frac{\delta_n}{\delta_c}\right), \tag{4}$$

where $\sigma_c$ represents material strength. The effective formulation was first proposed by Camacho and Ortiz [6].

The tangent modulus (cohesive material Jacobian) matrix is obtained from differentiating tractions, i.e. $t_s$ and $t_n$, with respect to relative displacements, i.e. $\delta_s$ and $\delta_n$. For $\lambda_e < \lambda_{cr}$, the tangent modulus matrix components are given as

$$C_{ss} = \frac{\partial t_s}{\partial \delta_s} = C_{nn} = \frac{\partial t_n}{\partial \delta_n} = \frac{\sigma_c}{\lambda_{cr}\delta_c} \tag{5}$$

$$C_{sn} = \frac{\partial t_s}{\partial \delta_n} = C_{ns} = \frac{\partial t_n}{\partial \delta_s} = 0 \tag{6}$$

and for $\lambda_e > \lambda_{cr}$, they are given as

$$C_{ss} = \frac{\partial t_s}{\partial \delta_s} = -\frac{\delta_c\sigma_c}{1-\lambda_{cr}}\left(\frac{\delta_s}{\lambda_e\delta_c^2}\right)^2 + (1-\lambda_e)\frac{\delta_c\sigma_c}{1-\lambda_{cr}}\left(\frac{1}{\lambda_e\delta_c^2} - \frac{1}{\lambda_e^3}\frac{\delta_s^2}{\delta_c^4}\right) \tag{7}$$

$$C_{sn} = \frac{\partial t_s}{\partial \delta_n} = C_{ns} = \frac{\partial t_n}{\partial \delta_s} = -\frac{\delta_c\sigma_c}{1-\lambda_{cr}}\left(\frac{\delta_s}{\lambda_e\delta_c^2}\right)\left(\frac{\delta_n}{\lambda_e\delta_c^2}\right) + (1-\lambda_e)\frac{\delta_c\sigma_c}{1-\lambda_{cr}}\left(-\frac{1}{\lambda_e^3}\frac{\delta_s\delta_n}{\delta_c^4}\right) \tag{8}$$

$$C_{nn} = \frac{\partial t_n}{\partial \delta_n} = -\frac{\delta_c\sigma_c}{1-\lambda_{cr}}\left(\frac{\delta_n}{\lambda_e\delta_c^2}\right)^2 + (1-\lambda_e)\frac{\delta_c\sigma_c}{1-\lambda_{cr}}\left(\frac{1}{\lambda_e\delta_c^2} - \frac{1}{\lambda_e^3}\frac{\delta_n^2}{\delta_c^4}\right). \tag{9}$$

The cohesive fracture energy is computed by equating the area under the displacement-traction curve (see Fig. 1), namely,

$$G_c = \frac{1}{2}\delta_c\sigma_c. \tag{10}$$

The traction vector and tangent modulus matrix are functions of displacements, cohesive parameters and internal variables. The cohesive parameters and internal variables are constant at each increment. However, the displacement, the traction and the tangent modulus matrix need to be updated at each increment. Detailed numerical aspects of CZM implementation via the UEL capability in ABAQUS are presented in the next section.

### 2.2. Finite element implementation

This section describes how the bilinear CZM presented in the previous section is incorporated into the ABAQUS user element (UEL) [25]. In the UEL, the contribution of cohesive elements to the force vector and the tangent stiffness matrix, which are functions of displacements, cohesive parameters and internal variables, should be defined. Because the force vector and the tangent stiffness matrix need to be defined globally, while the cohesive law represents a local separation and traction relationship, transformation between global and local coordinates is necessary. Consider the 4-noded cohesive element shown in Fig. 2. The parameter $\theta$ represents the angle between global and local coordinates. $X$ and $Y$ denote global coordinates, while $s$ and $n$ indicate local coordinates. Nodes 1 and 2 are located on the bottom of the element whereas nodes 3 and 4 are located on the top of the element. Each node has two degrees of freedom. The global displacement vector of the nodes belonging to the cohesive element can be expressed as follows:

$$\boldsymbol{u}_g = \begin{bmatrix} u_X^1 & u_Y^1 & u_X^2 & u_Y^2 & u_X^3 & u_Y^3 & u_X^4 & u_Y^4 \end{bmatrix}^T, \tag{11}$$

where superscripts indicate node numbers, subscripts $X$ and $Y$ denote global degrees of freedom, and subscript $g$ refers to the global coordinate system.

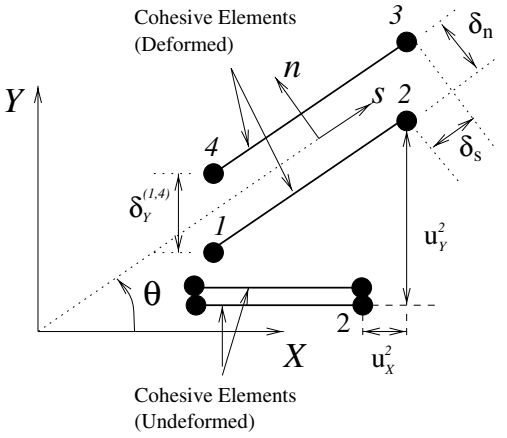


Fig. 2. Schematic drawing of a 4-noded linear cohesive element. Variables $\delta_s$ and $\delta_n$ represent shear sliding and normal displacement jump, respectively. Variables $u_X^2$ and $u_Y^2$ denote global displacements of node 2 along $X$ and $Y$ directions, respectively. The variable $\delta_Y^{(1,4)}$ represents the opening displacement between nodes 1 and 4 along global $Y$ direction, while $\theta$ indicates the angle between global and local coordinates. Notice that $X$ and $Y$ denote global coordinates, whereas $s$ and $n$ denote local coordinates.

The global relative displacements, i.e. $\delta_X$ and shear sliding $\delta_Y$, between top and bottom nodes can be obtained as

$$\begin{Bmatrix} \delta_X^{(1,4)} \\ \delta_Y^{(1,4)} \\ \delta_X^{(2,3)} \\ \delta_Y^{(2,3)} \end{Bmatrix} = \boldsymbol{L}\boldsymbol{u}_g, \quad \boldsymbol{L} = \begin{bmatrix} 1 & 0 & 0 & 0 & 0 & 0 & -1 & 0 \\ 0 & 1 & 0 & 0 & 0 & 0 & 0 & -1 \\ 0 & 0 & 1 & 0 & -1 & 0 & 0 & 0 \\ 0 & 0 & 0 & 1 & 0 & -1 & 0 & 0 \end{bmatrix}, \tag{12}$$

where $\boldsymbol{L}$ is the operator matrix, and superscripts denote corresponding nodes of the cohesive element for which cohesive separation will be enforced (see Fig. 2). The relative global displacement at Gauss points can be obtained as follows:

$$\begin{Bmatrix} \delta_X \\ \delta_Y \end{Bmatrix} = \begin{bmatrix} N_1 & 0 & N_2 & 0 \\ 0 & N_1 & 0 & N_2 \end{bmatrix} \begin{Bmatrix} \delta_X^{(1,4)} \\ \delta_Y^{(1,4)} \\ \delta_X^{(2,3)} \\ \delta_Y^{(2,3)} \end{Bmatrix} = \boldsymbol{N} \begin{Bmatrix} \delta_X^{(1,4)} \\ \delta_Y^{(1,4)} \\ \delta_X^{(2,3)} \\ \delta_Y^{(2,3)} \end{Bmatrix} = \boldsymbol{N}\boldsymbol{L}\boldsymbol{u}_g. \tag{13}$$

Note that $\delta_X$ and $\delta_Y$ require transformation from global coordinates to a local coordinate system for the cohesive element. Let matrix $\boldsymbol{R}$ define the orthogonal transformation from global reference frame $(X, Y)$ to the element specific, local coordinate system $(s, n)$, where the direction $n$ lies normal to the cohesive element. Finally, the relative local displacement vector, $\delta_s$ and $\delta_n$, is obtained as follows:

$$\begin{Bmatrix} \delta_s \\ \delta_n \end{Bmatrix} = \boldsymbol{B}\boldsymbol{u}_g = \boldsymbol{R}\boldsymbol{N}\boldsymbol{L}\boldsymbol{u}_g. \tag{14}$$

The global nodal force vector and global tangent stiffness matrix for a 4-noded cohesive element can be evaluated as:

$$\boldsymbol{f} = \int_{-1}^{1} \boldsymbol{B}^{\mathrm{T}}\boldsymbol{t}J_0 \mathrm{d}\eta, \quad \boldsymbol{K} = \int_{-1}^{1} \boldsymbol{B}^{\mathrm{T}}\boldsymbol{C}\boldsymbol{B}J_0 \mathrm{d}\eta, \tag{15}$$

where $J_0$ denotes the Jacobian between reference and original coordinates. Notice that the traction ($\boldsymbol{t}$) and the tangent modulus matrix ($\boldsymbol{C}$) are evaluated using Eq. (3) through Eq. (9).

Table 1
Various approaches for cohesive zone fracture modeling in asphalt concrete

| | Bulk (background) | Cohesive (fracture) | References |
|---|---|---|---|
| Case 1 | No rate effects | No rate effects | [20,23] |
| Case 2 | Rate effects | No rate effects | Present paper |
| Case 3 | No rate effects | Rate effects | [26] |
| Case 4 | Rate effects | Rate effects | [26] |

A library of cohesive elements is available in version 6.5 of ABAQUS [25], which include bilinear cohesive elements. However, the present implementation has been done independently of ABAQUS library of cohesive elements. One of the advantages of the present UEL implementation is the potential extension of the model to consider rate dependency. This study of rate effects on fracture behavior is beyond the scope of this paper and will be addressed in future work [26] (see Table 1).

## 3. CZM compliance issues

In this section, the effect of cohesive law compliance is explored in the context of its applicability for fracture studies involving asphalt concrete. Furthermore, two cohesive zone models, i.e. a potential-based cohesive zone model [5] and a bilinear model [8], are employed to investigate the influence of the model on the compliance simulating a one-dimensional problem [27] and a two-dimensional SE(B) test. For simplicity, rate-independent constitutive models for both the bulk and cohesive materials are used in this section.

Fig. 3 illustrates the simple one-dimensional problem with bulk and cohesive elements. $F$ denotes the force, $h$ is the length of the bulk material, $u$ is the stretch of the bulk material, $\delta_n$ is the displacement jump between the cohesive surfaces, and $A$ is the area of the block upon which $F$ is applied. Imposing an equilibrium condition between bulk and cohesive elements with unit area $A$ [27], one obtains

$$E\varepsilon = k\delta_n, \tag{16}$$

where $E$ is Young's modulus, $\varepsilon$ is strain of the bulk material and $k$ is a constant of proportionality between displacement jump and the corresponding traction, i.e. stiffness. Combining $\varepsilon = u/h$ and $E_e = \sigma/\varepsilon_{tot} = \sigma h/(u + \delta_n)$ with Eq. (16), one obtains the effective modulus under mode I loading as follows:

$$E_e = E\varepsilon\frac{h}{u+\delta_n} = E\frac{h}{h+E/k} = E\left[1-\frac{1}{1+\frac{kh}{E}}\right] = E\left[1-\frac{1}{1+\frac{\sigma_c}{E}\frac{h}{\delta_c}}\right], \tag{17}$$

where $\sigma_c$ and $\delta_c$ denote the maximum traction (finite material strength) and the corresponding displacement of the cohesive law, respectively.

Fig. 4 shows the effective modulus of a one-dimensional specimen as a function of $h$, $\delta_c$, and $\sigma_c$. From this result, we observe that as the ratios $\sigma_c/E$ and $h/\delta_c$ increase, the compliance owing to the elasticity of the cohesive law is negligible indicating that the effective modulus ($E_e$) of the specimen approaches the properties of the continuum ($E$). This is intuitive because as the ratio of $\sigma_c/E$ and $h/\delta_c$ increases, the relative contribution of

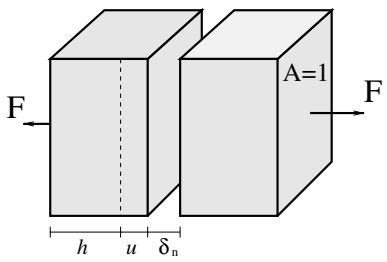


Fig. 3. One-dimensional problem with bulk and cohesive elements.

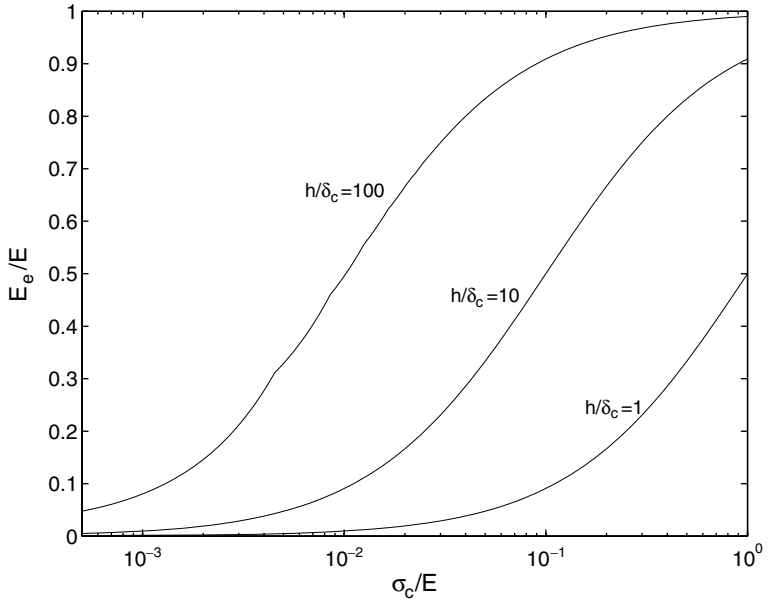


Fig. 4. Effective modulus as a function of $h$, $\delta_c$, and $\sigma_c$.

cohesive elements to global responses decreases, and as a result, the amount of artificially induced compliance becomes small.

In order to correlate material properties of asphalt concrete and the compliance of the cohesive models, two cohesive models [5,8] are employed. Identical material properties are used in the comparison of the two models, namely: $E = 14.2$ GPa, $v = 0.35$, $\sigma_c = 3.56$ MPa and $G_c = 344$ J m$^{-2}$. These properties were measured from samples of asphalt concrete tested as part of the design of a surface mixture for the rehabilitation of taxiway E at the Greater Peoria (Illinois) Regional Airport in 2001. The effective modulus of the exponential model [5] and bilinear model [8] as a function of $h$ and $\delta_c$ is plotted in Fig. 5. Significant compliance is induced

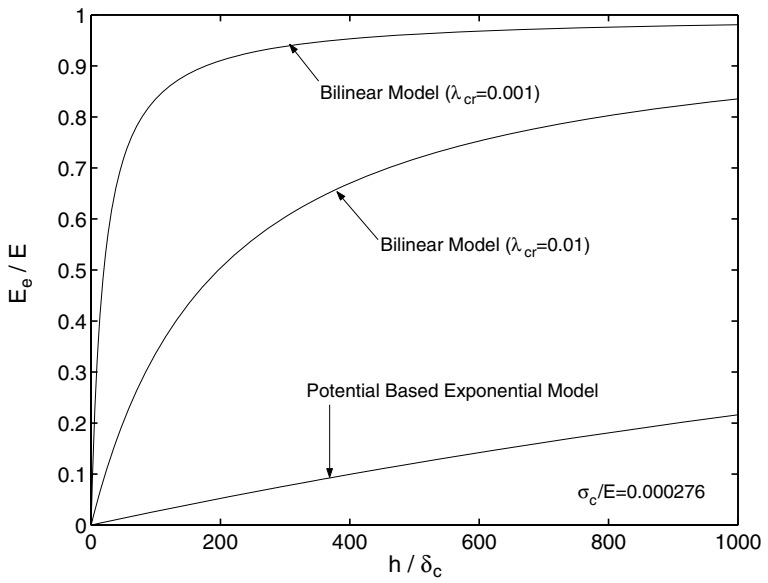


Fig. 5. Effective modulus as a function of $h$ and $\delta_c$ using bilinear and exponential cohesive zone models [5,8] for asphalt concrete material properties.

due to the low ratio of $\sigma_c/E$, e.g. $\sigma_c/E = 0.000276$, when the exponential model is adopted. A considerable reduction of compliance results when the bilinear model is employed. Moreover, the effective modulus ($E_e$) approaches the properties of continuum ($E$) as $\lambda_{cr}$ decreases.

To investigate further the compliance of the cohesive laws [5,8] using asphalt concrete materials, a simulation of a recently developed SE(B) test for asphalt concrete is performed. Fig. 6(a) illustrates a simply supported SE(B) with a length of 376 mm, a height of 100 mm and a thickness of 75 mm. The simulated mechanical notch extends 19 mm from the bottom edge of the beam. External loading is imposed at the center of the top edge of the model. Fig. 6(b) shows the finite element configuration for the whole geometry, which is constructed using 28112 3-noded triangular plane strain elements. Fig. 6(c) illustrates mesh details for the regions where cohesive elements are inserted. Three different cases are considered. In the first case, cohesive elements are inserted only along the center of the specimen with 800 4-noded linear cohesive elements. In the second case, cohesive elements are inserted over central region of the specimen between $(-0.2, 19.0)$ and $(0.2, 99.2)$ with 13236 4-noded linear cohesive elements. Finally, in the third case cohesive elements are inserted between $(-9.2, 19.0)$ and $(9.2, 99.2)$ with 32186 4-noded linear cohesive elements. Notice that the number of cohesive elements used in cases II and III is approximately 15 and 40 times, respectively, larger than that of case I.

Force ($P$) versus crack mouth opening displacement (CMOD) curves using the exponential model and the bilinear model for case I are plotted in Fig. 7(a). For comparison purposes, the $P$ versus CMOD curve

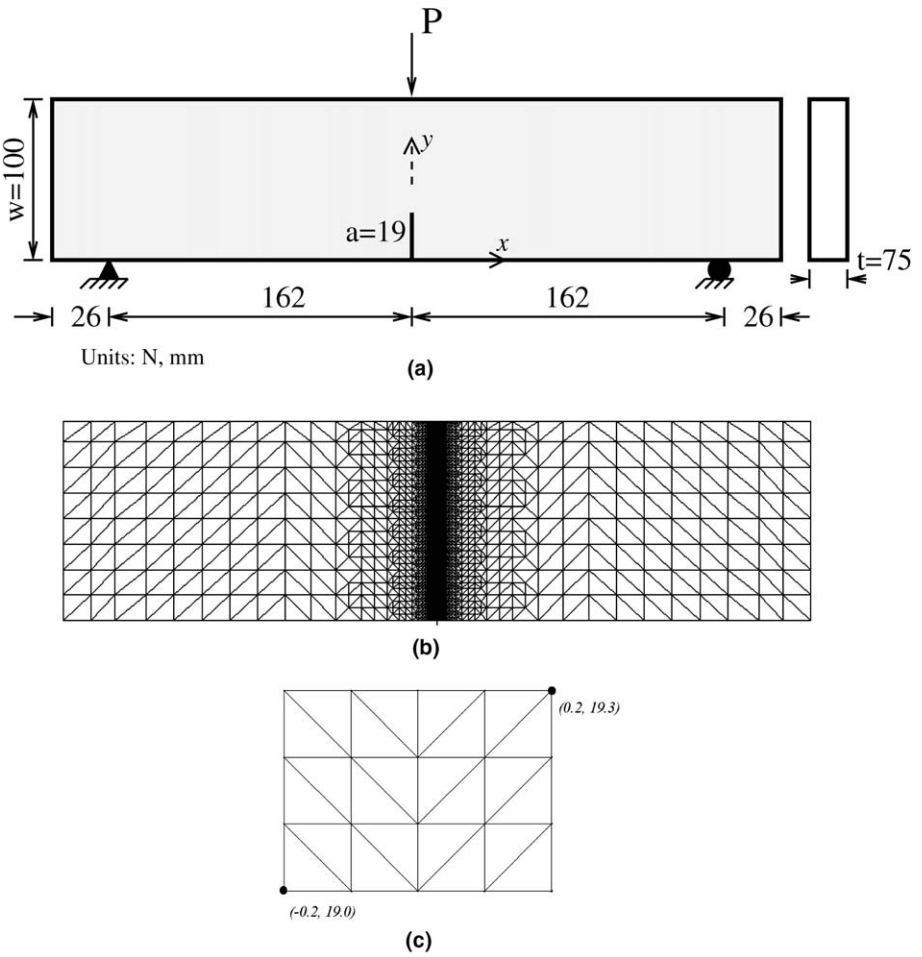


Fig. 6. SE(B) test simulation: (a) geometry and boundary conditions; (b) mesh configuration for the whole geometry; and (c) mesh details for the regions where cohesive elements are inserted.

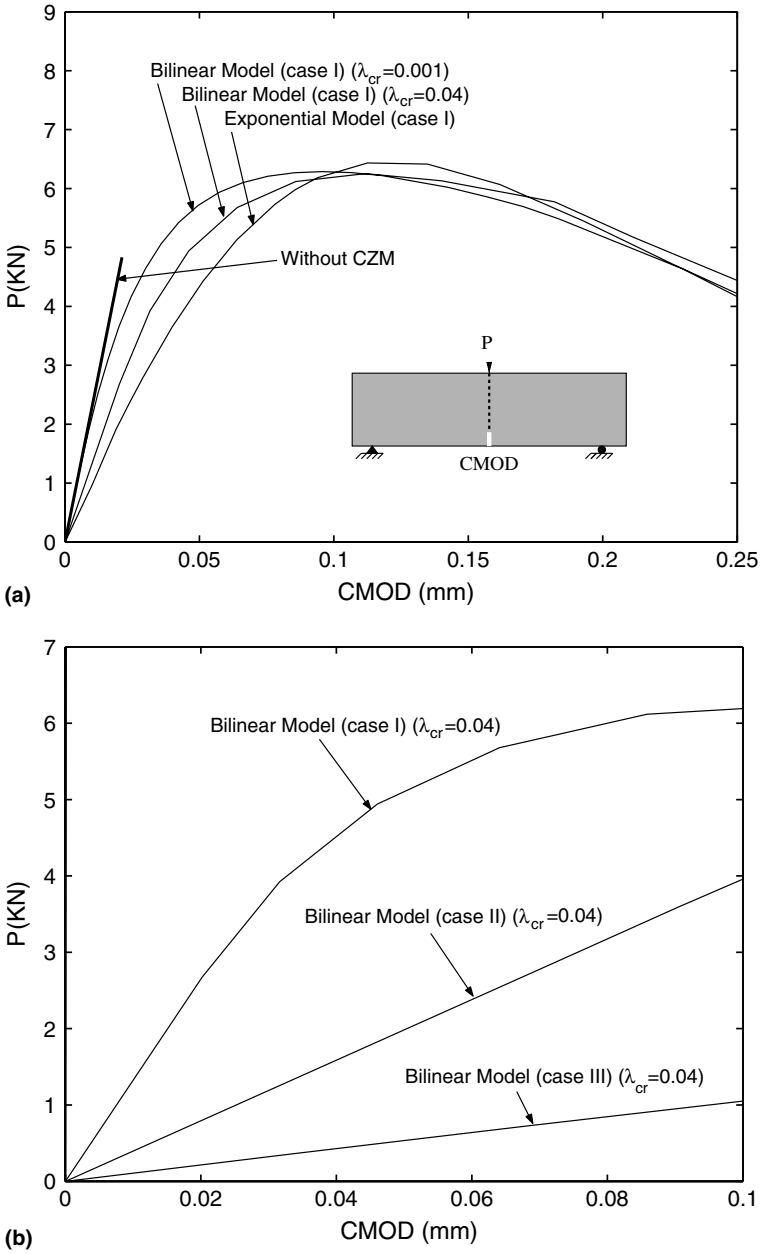


Fig. 7. Comparison of $P$ versus CMOD curves: (a) using cohesive zone models [5,8] for the case I; and (b) using the bilinear model [8] for the three cases.

obtained when cohesive elements are not used is plotted, which establishes a baseline corresponding to zero artificially-induced compliance. When the bilinear model is adopted, the compliance is reduced tremendously. Moreover, the influence of $\lambda_{cr}$ in the bilinear model is noteworthy. To examine the relationship between number of cohesive elements and compliance, $P$ versus CMOD curves using the bilinear model for the three cases are plotted in Fig. 7(b). It is clearly observed that as the number of cohesive elements increases, the compliance likewise increases. This is intuitive because as the number of cohesive elements increases, the contribution of the cohesive elements in terms of the compliance likewise increases. Thus, it is recommended to minimize the number of cohesive elements, if possible, and to adopt cohesive zone models which can control a pre-peak slope, e.g. a bilinear CZM, when modeling fracture in asphalt concrete.

## 4. Viscoelasticity

In this section, a basic introduction to the viscoelastic constitutive laws used in this study is first provided. Then, energy balance is presented in conjunction with the computational simulation.

### 4.1. Basic formulation

The constitutive law for isotropic viscoelasticity in the form of a hereditary integral formulation is [25,28,29]

$$\boldsymbol{\sigma}(t) = \int_0^t 2G(\xi - t')\dot{\boldsymbol{e}}\mathrm{d}t' + \boldsymbol{I}\int_0^t K(\xi - t')\dot{\phi}\mathrm{d}t', \tag{18}$$

where $K$ and $G$ are bulk and shear moduli, respectively, which are functions of the reduced time, $\xi$, which is later described in this section. The superscripted dots denote differentiation with respect to time $t'$, while $\phi$ and $\boldsymbol{e}$ are the mechanical volumetric and deviatoric strains, respectively, given as

$$\phi = \varepsilon_{kk} \quad \text{and} \quad e_{ij} = \varepsilon_{ij} - 1/3\delta_{ij}\phi, \tag{19}$$

in which $\delta_{ij}$ denotes Kronecker delta. The bulk ($K$) and shear ($G$) moduli can be defined individually using Prony series representation

$$K(\xi) = K_\infty + \sum_{i=1}^{n_k} K_i \exp(-\xi/\tau_i^K) \quad G(\xi) = G_\infty + \sum_{i=1}^{n_G} G_i \exp(-\xi/\tau_i^G), \tag{20}$$

where $K_\infty$ and $G_\infty$ are the long term bulk and shear moduli, respectively. In general, the material has a different relaxation time of $\tau_i^K$ and $\tau_i^G$, and different moduli of $K_i$ and $G_i$, and a variable number of Prony series parameters ending in $n_K$ and $n_G$. In this study, all relaxation is assumed to occur in the shear mode [30].

In order to obtain the relaxation modulus, two approaches are generally considered. The first is to conduct a relaxation test, where constant strain is imposed and a generalized Maxwell model is used to describe the resulting material response. The second is to conduct a creep test, where constant stress is imposed and a Voight–Kelvin model is used to describe creep compliance behavior, which is then used to obtain relaxation modulus using interconversion schemes [31,32]. In asphalt concrete, the second approach is preferable due to several reasons, e.g. a constant stress creep test is easier to perform than the constant strain relaxation test [31].

The creep compliance function using a Voight–Kelvin model is given as

$$D(\xi) = D(0) + \sum_{i=1}^{N} D_i(1 - \mathrm{e}^{-\xi/\tau_i}) + \frac{\xi}{\eta_v}, \tag{21}$$

where $\xi$ is reduced time, $D(\xi)$ is creep compliance at the reduced time, and $D(0)$, $D_i$, $\tau_i$ and $\eta_v$ are model constants. The reduced time $\xi$ is obtained from $t/a_\mathrm{T}$ where $t$ is a real time and $a_\mathrm{T}$ is a temperature shift factor. Model constants are obtained from creep tests conducted at multiple temperatures, and shift factors are evaluated from shifting compliance versus time curve at different temperatures in log scale to establish a smooth, continuous curve. In this study, the creep compliance for the mixture was measured at −20, −10, and 0 °C using the Superpave IDT test [33,34].

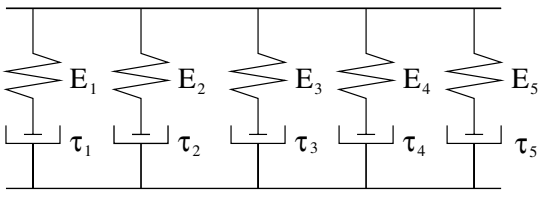


Fig. 8. Viscoelasticity in asphalt concrete: generalized Maxwell model (10 parameters) for viscoelastic characterization.

Interconversion of the time dependent creep compliance function of Eq. (21) yields a relaxation modulus given as

Table 2
Prony series parameters for the master relaxation modulus using the generalized Maxwell model [35]

| $i$ | Relaxation modulus parameters | |
|---|---|---|
| | $E_i$ (GPa) | $\tau_i$ (s) |
| 1 | 3.4 | 12 |
| 2 | 3.4 | 162 |
| 3 | 5.9 | 1852 |
| 4 | 6.8 | 17476 |
| 5 | 6.1 | 465460 |

Table 3
Temperature shift factors [35]

| Temperatures (°C) | $\log(1/a_T)$ |
|---|---|
| −20 | 0 |
| −10 | 1.34 |
| 0 | 2.70 |

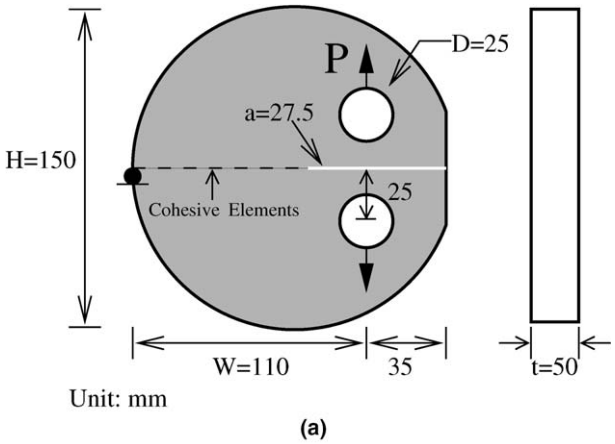


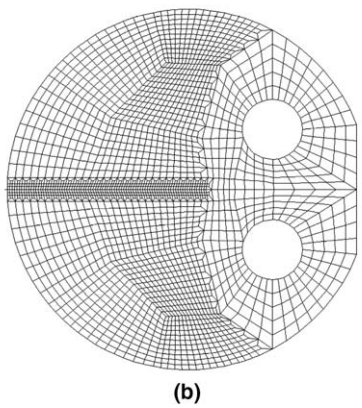


Fig. 9. DC(T) test simulation; (a) geometry and boundary conditions and (b) mesh configurations for the whole geometry.

$$E(\xi) = \sum_{i=1}^{N+1} E_i e^{-\xi/\tau_i}, \tag{22}$$

where $E(\xi)$ is a relaxation modulus at the reduced time of $\xi$, and $E_i$ and $\tau_i$ are model constants for the master relaxation modulus curve. Fig. 8 shows a generalized Maxwell model, which is a widely used constitutive model to describe the linear viscoelastic behavior of asphalt concrete. Tables 2 and 3 contain the generalized Maxwell model parameters and shift factors, respectively. Notice that bulk and cohesive material properties employed in the remainder of simulations are based on a typical surface mixture used in central Illinois in which the binder grade is PG 64-22 and a nominal maximum aggregate size (NMAS) of 9.5 mm is used [35].

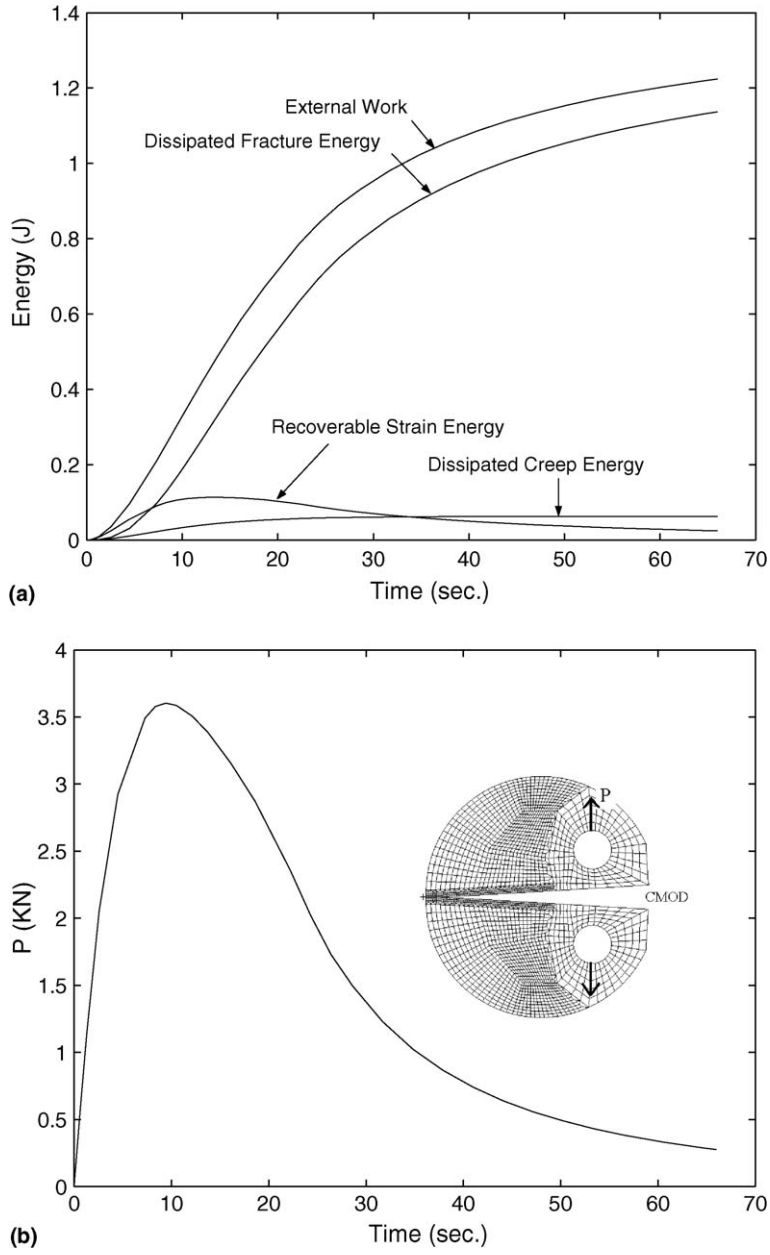


Fig. 10. DC(T) simulation: (a) energy balance with 1.0 *mm/min*. CMOD loading rate at −10 °C and (b) a load versus time curve.

### 4.2. Energy balance

Wagoner et al. [36,37] proposed the disk-shaped compact tension test, or DC(T), for asphalt concrete. Fig. 9(a) illustrates a DC(T) specimen which is 150 mm high, 145 mm long and 50 mm thick. The length of the mechanical notch is 27.5 mm, leading to $a/w = 0.25$. Loading pins are inserted in the holes and pulled apart with a closed-loop servohydraulic loading system to induce opening. Fig. 9(b) shows mesh discretizations for the whole geometry. The DC(T) test specimen is constructed using 2376 4-noded quadrilateral plane strain elements for the bulk elements and 88 4-noded linear elements for the cohesive elements. The cohesive elements are inserted along the middle of specimen to enable the simulation of pure mode-I crack propagation. Cohesive elements of 1.0 mm size are employed, as these are found through parametric investigation to be small enough to capture nonlinear softening behavior occurring in the cohesive zone [23]. A constant Poisson's ratio is used: $v = 0.35$. The cohesive fracture energy obtained at $-10$ °C and 1 mm min$^{-1}$. CMOD loading rate is 324 J m$^{-2}$ ($G_c = 324$ J m$^{-2}$), and the material strength measured at $-10$ °C is 3.58 MPa ($\sigma_c = 3.58$ MPa) [35]. The instantaneous modulus and the modulus at 60 s and $-10$ °C are 25.6 GPa and 11.9 GPa, respectively.

Fig. 10(a) shows energy components for a DC(T) test simulation with a controlled CMOD rate of 1 mm min$^{-1}$ loading rate and material parameters associated with $-10$ °C. The abscissa represents time and the ordinate denotes components of total energy. The total dissipated fracture energy is computed as part of the UEL and is given as, under mode-I condition,

$$E^{\mathrm{f}} = \sum \int \int t_{\mathrm{n}} \mathrm{d}\delta_{\mathrm{n}} \mathrm{d}A, \tag{23}$$

where superscript f denotes fracture, $A$ represents area, and $\delta_{\mathrm{n}}$ and $t_{\mathrm{n}}$ denote normal opening displacement and the corresponding normal traction between a cohesive element, respectively. As illustrated in Fig. 10(a), dissipated fracture energy increases as time increases, which is expected. However, recoverable strain energy and dissipated creep energy show different behavior. As time increases, recoverable strain energy increases, reaches peak point around 10 s and then decays as the crack extends through the specimen. This trend is almost identical with that of load versus time as illustrated in Fig. 10(b). On the other hand, the creep energy dissipation increases gradually before 40 s and shows a steady-state trend after 40 s. The contribution of recoverable strain energy, dissipated creep energy and dissipated fracture energy to the total work is 35%, 10% and 55%, respectively at 10 s, and 2%, 5% and 93%, respectively at 60 s.

## 5. Numerical results

Considering viscoelastic bulk materials, simulation of crack propagation in the mode I DC(T) and mixed-mode SE(B) tests are carried out using the bilinear cohesive zone model. In the DC(T) test, the cohesive parameters are calibrated by matching numerical results with experimental results. In the mixed-mode SE(B) simulation, cohesive elements with a regular pattern are inserted over an area to allow cracks to grow in any direction and to minimize the influence of mesh discretization on crack trajectory. The crack trajectory obtained from the aforementioned mixed-mode simulation is then compared with that of experimental results. Moreover, discussion on numerical convergence with several different finite element discretizations is presented.

### 5.1. Calibration of cohesive parameters in the DC(T)

In the nonlinear cohesive constitutive model, the cohesive fracture energy and the material strength are the main parameters used in this study. While these parameters obtained from experiments reflect viscoelastic heterogeneous material, in the current modeling viscoelastic effects are considered in bulk elements only and the bulk and cohesive elements are assumed to be homogeneous. Furthermore, a cohesive fracture energy obtained from equating to an area of a force versus CMOD curve may overestimate the local work of separation, because CMOD is a combination of both the bulk and fracture responses [38]. As a result, model

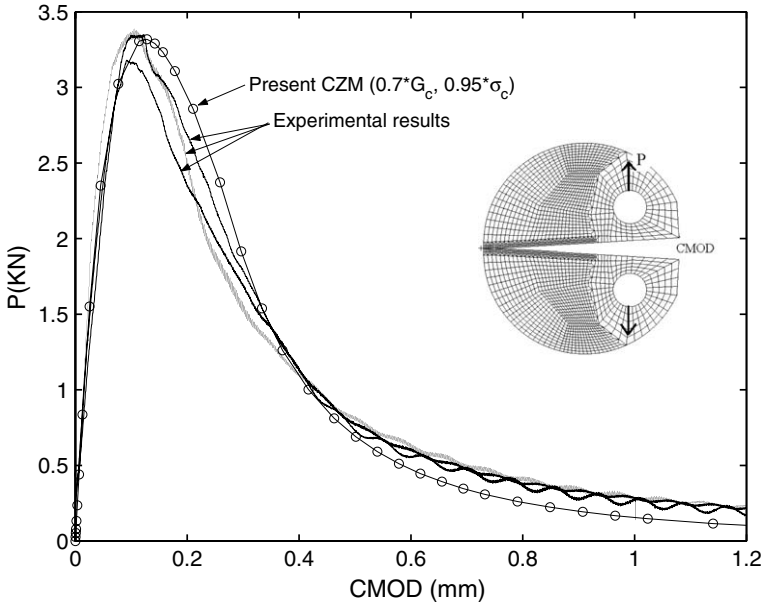


Fig. 11. Comparison of $P$ versus CMOD curves between numerical and experimental results [37].

calibration is necessary. In this work, cohesive parameters are calibrated by fitting present numerical results to experimental results in order to account for the differences between experiments and numerical simulations.

Fig. 11 compares the present numerical results with experimental results. The abscissa indicates CMOD (mm) and the ordinate indicates the load $P(KN)$. Three specimens are tested at $-10$ C and 1 mm/min. CMOD loading rate. Detailed procedures for the DC(T) test are described by Wagoner et al. [36]. The predicted $P$ versus CMOD curve matches favorably with that of experimental results. Relatively small calibration shifts of cohesive parameters, i.e. $0.7G_c = 0.7 \times 324$ J m$^{-2}$ and $0.95\sigma_c = 0.95 \times 3.58$ MPa, are required to bring simulated results into reasonable comparison with measured results. For the remainder of simulations, the calibrated cohesive parameters are adopted.

### 5.2. Mixed-mode crack propagation in the SE(B)

Unlike the previous example (mode I) where a crack path is predefined, in the simulation of mixed-mode fracture in the SE(B) test cohesive elements are inserted over an area to allow cracks to propagate in any direction. Fig. 12(a) shows the geometry, boundary condition, and shaded region where cohesive elements have been inserted. The length, height and thickness of the SE(B) specimen are 376 mm, 100 mm and 75 mm, respectively. The notch tip is located at 65 mm left and 19 mm above the center of the bottom edge of the beam. External loading is imposed at the center of the top edge of the model for the mid-span loading configuration of the SE(B) test. Figs. 12(b) and (c) illustrate finite element discretization for the entire model along with mesh details in the shaded region where cohesive elements are inserted. The shaded region between (123, 19) and (150, 95) is constructed in a regular pattern with 3-noded triangular elements having an aspect ratio of 1:1.9 ($x$:$y$). The SE(B) structure is constructed using 5398 3-noded triangular elements for bulk material and 3066 4-noded linear elements for cohesive interfaces. A viscoelastic analysis is performed. We assume the same cohesive fracture energy for mode-I and mode-II.

Fig. 13(a) illustrates the final deformed shapes and crack trajectories from the simulation. A magnification factor of 30 is used to make crack trajectories visible. Fig. 13(b) shows a comparison of the crack trajectories of experimental and numerical results. Green and blue lines indicate the crack trajectories of the experimental results and a red line indicates the crack trajectory of the present numerical simulation, indicating favorable agreement.

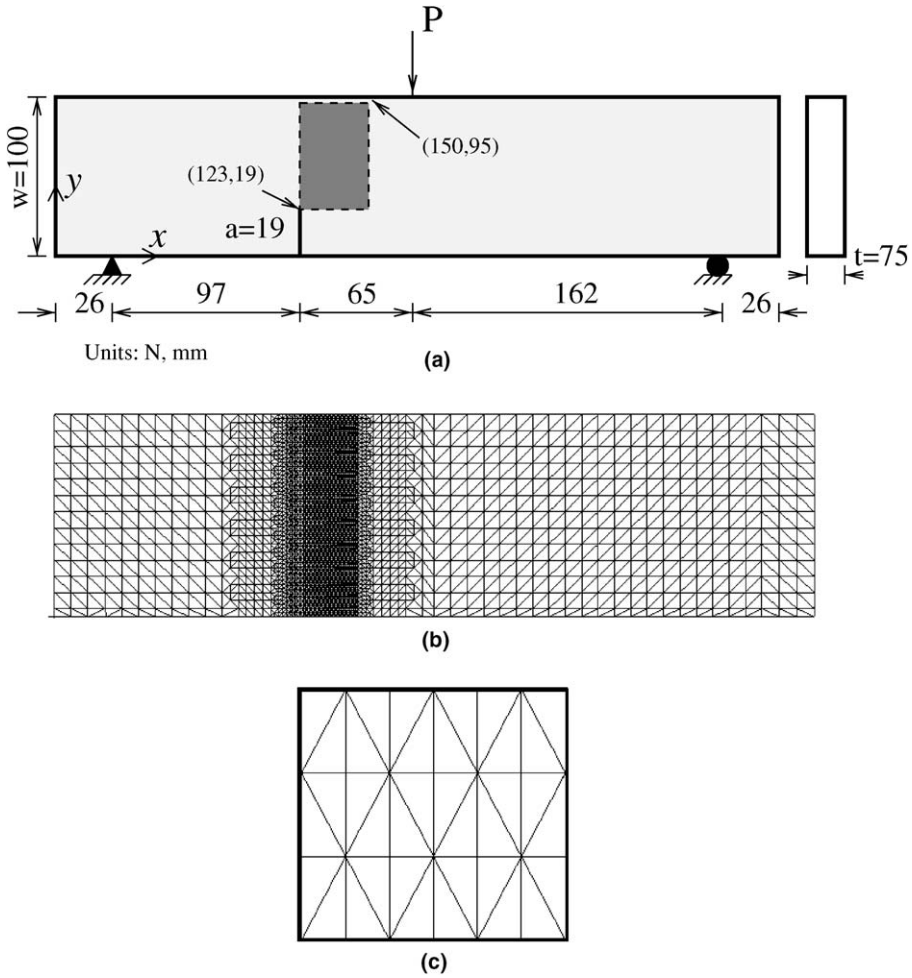


Fig. 12. Mixed-mode SE(B) test: (a) geometry and boundary conditions; (b) mesh configuration for the whole geometry; and (c) mesh details of the shaded region of (123,19) and (150,95) where cohesive elements are inserted.

### 5.3. Discussion on numerical convergence

It has been reported that one of the challenges in cohesive zone modeling is lack of numerical convergence when an implicit displacement-based finite element scheme is used. This problem is rarely observed when cohesive elements are inserted along a predefined line. Numerical non-convergence, however, is pronounced when a number of cohesive elements are inserted over an area in the absence of known crack paths. In this section, numerical convergence is presented and discussed in context of mesh discretization and nonlinear equation solvers. For simplicity, viscoelastic effects are not considered in this portion of study.

Several researchers [39–41] have explored integration schemes and/or nonlinear equation solvers to enhance convergence when using cohesive zone models. Regarding integration schemes, Roy and Dodds [39] reported that the Newton–Cotes integration rule leads to oscillatory opening profiles and induces numerical divergence, indicating that conventional Gauss Quadrature is superior to the Newton–Cotes. Han et al. [40] adopted a Lobatto $3 \times 3$ numerical integration for interface elements to avoid numerical divergence for three-dimensional problems. Regarding nonlinear equation solvers, several researchers adopted arc-length methods to overcome non-convergence in conjunction with cohesive elements [40,41]. The arc-length method, initially proposed by Riks [42] and modified by other researchers [43,44] succeeded in tracing the limit point and post peak responses by a prescribed arc-length. However, the arc-length method still fails to converge at or near the

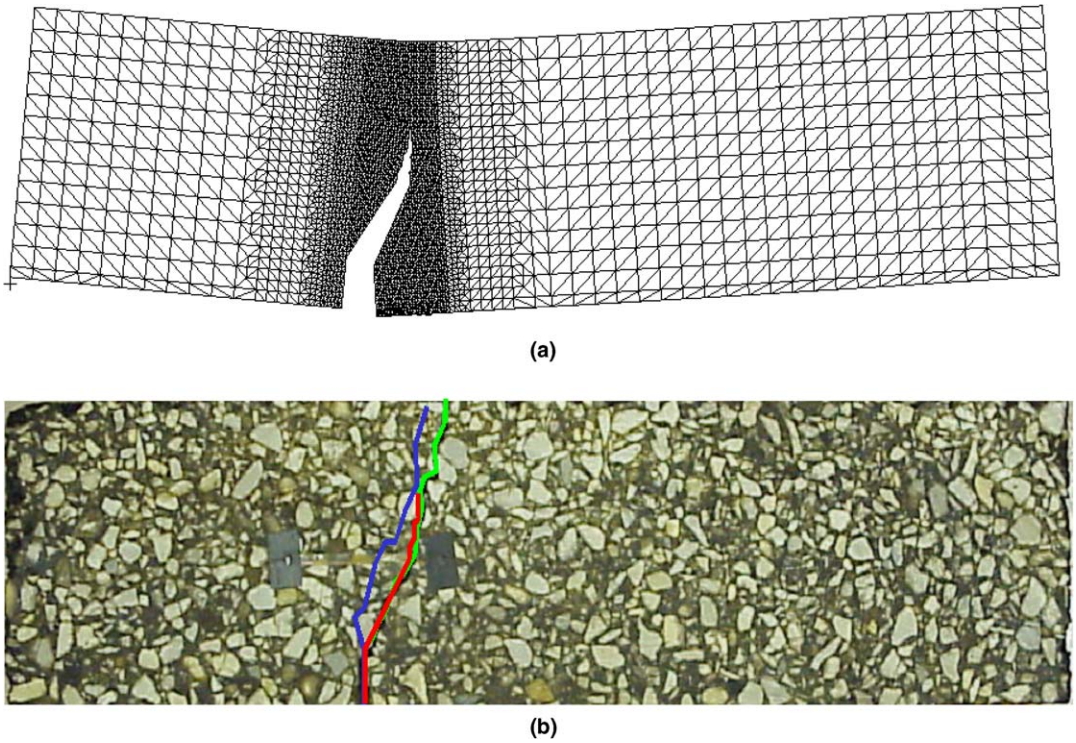


Fig. 13. Simulation of the mixed-mode SE(B) test: (a) deformed shape showing crack trajectory (scale factor is 30) and (b) comparison of the crack trajectory between numerical and experimental results. Red line indicates the crack trajectory obtained from the present numerical simulation, and green and blue lines denote the crack trajectories from the experiment. (For interpretation of the references to colour in this figure legend, the reader is referred to the electronic version of this article.)

limiting points. Rots and de Borst [41] pointed out that "this instability should be attributed to the global constraints equations including all the degree of freedom, which was contradictory to the fact that the failure zone or fracture process zone is highly localized."

To address and clarify these numerical issues associated with the CZM, crack propagation analysis of the mixed-mode SE(B) test is performed. The geometry, boundary conditions and cohesive parameters of SE(B) test are identical with those of SE(B) test in Section 5.2 (see Fig. 12(a)). $E = 14.2$ GPa and $v = 0.35$ are used. The three different mesh discretizations are adopted to study the influence of mesh discretization on the numerical convergence (see Figs. 14(a), (d) and (g)). Furthermore, two nonlinear solvers, i.e. the Newton–Raphson and Riks methods, are employed to explore their influence on the convergence. Notice that the meshes of Figs. 14(a) and (d) are constructed in a regular pattern, while the mesh of Fig. 14(g) is tailored to the crack trajectory predicted using a discrete fracture approach with the program I-FRANC2D [45].

Fig. 14 illustrates the final crack trajectory for different mesh discretizations using two nonlinear solvers before the solutions experience divergence. The bottom-left point in each deformed shape corresponds to the original crack tip and the top-right point corresponds to the location of external loading. Figs. 14 (a), (d) and (g) illustrate mesh details for Figs. 14(b) and (c), (e) and (f), and (h) and (i), respectively. Several important observations from this analysis include: (1) for the meshes constructed in a regular pattern, the Riks method yields better performance than the Newton–Raphson method with a varying degree of success depending on the mesh discretization; (2) for the mesh tailored to the crack trajectory predicted from I-Franc2D, both nonlinear solvers perform very well demonstrating that the degree of convergence depends upon the finite element discretizations. In other words, if the crack propagation angle and inclination of cohesive interface element is similar with that of either analytical or experimental results, the numerical solution converges relatively well; and (3) once crack branching occurs, numerical solutions are rarely converged. Peak loads and final loads before solutions diverge for Figs. 14(b), (c), (e), (f), (h) and (i) are shown in Table 4.

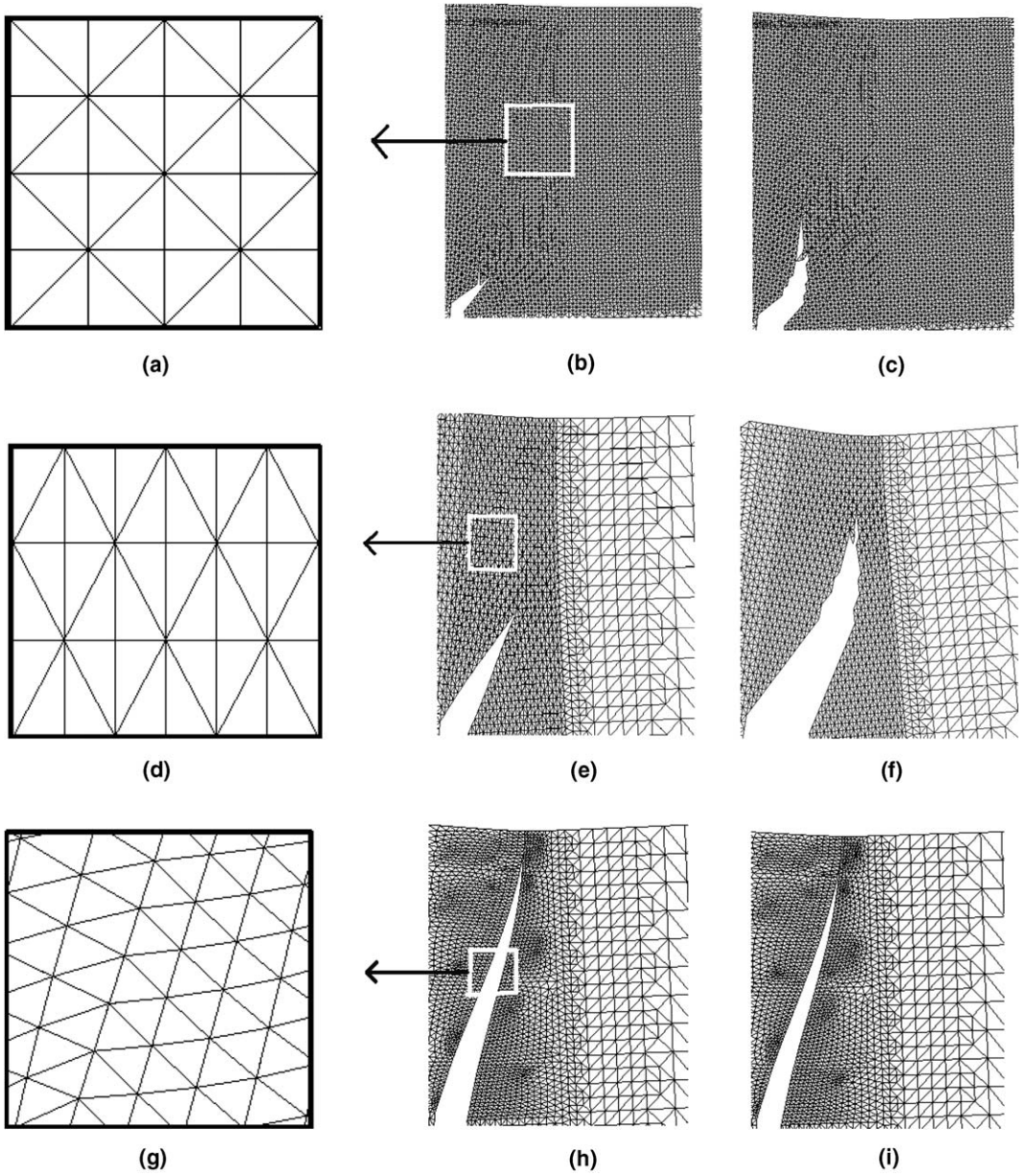


Fig. 14. Influence of mesh layout on convergence of the numerical solution and the crack pattern. Final crack trajectory: (a), (d) and (g) show mesh details for (b) and (c), (e) and (f), and (h) and (i), respectively. The Newton–Raphson is used for (b), (e) and (h), and the Riks method is adopted for (c), (f) and (i). Notice that the bottom left point of each deformed figure corresponds to the original crack tip and the top right point corresponds to the location of applied loading. Magnification factor 50 is used for (b), (c), (e) and (f), and the magnification factor 10 is employed for (h) and (i) to make crack trajectory visible.

Table 4
Loads associated to Fig. 14

| Mesh layout | (a) | | (d) | | (g) | |
|---|---|---|---|---|---|---|
| Final crack trajectory | (b) | (c) | (e) | (f) | (h) | (i) |
| Loads corresponding to final crack trajectory (KN) | 4.91 | 4.10 | 2.88 | 1.09 | 0.22 | 0.28 |
| Peak loads (KN) | – | 4.87 | 4.58 | 4.58 | 4.89 | 4.89 |

Notice that for Fig. 14(b), the numerical solution starts to diverge before it reaches the post-peak portion of the $P$ versus CMOD curve.

## 6. Summary and conclusions

In this study, a bilinear cohesive zone model is used for fracture modeling in asphalt concrete laboratory tests such as DC(T) and SE(B) considering viscoelastic effects in the bulk (background) material. In Section 1, a comprehensive review of the literature is presented. In Section 2, detailed theoretical and numerical aspects of the bilinear CZM are explained in conjunction with the ABAQUS user element subroutine (UEL) [25]. Detailed explanations regarding the computation of the force vector and the tangent stiffness matrix are presented. In Section 3, issues regarding compliance of the cohesive laws, i.e. the potential-based cohesive zone model [5] and the bilinear model [8], are explored by simulating a simple one-dimensional problem [27] and a two-dimensional SE(B) test in asphalt concrete. It is demonstrated that the bilinear cohesive zone model [8] is more appropriate for asphalt concrete materials than the model by Xu and Needleman [5] in terms of a reduction of compliance. In Section 4, energy balance is presented in conjunction with the computational simulation. In Section 5, simulation of the DC(T) fracture test is presented, in which the cohesive elements are inserted along the middle of the specimen to permit mode I crack propagation. This simulation is used to calibrate the cohesive zone model parameters. In the mixed-mode SE(B) test simulation, cohesive elements are inserted over an area to allow cracks to grow in any direction. Moreover, a regular finite element discretization is used to lower the influence of mesh discretization on crack trajectory. A mixed-mode crack propagation simulation is performed with good successes. However, it is observed that a numerical divergence is not avoidable for mixed-mode simulations, and highly depends upon the nature of the finite element discretization used. The mixed-mode crack trajectory from the present simulation is found to match remarkably well with experimental results.

The major contributions of this study can be summarized as follows:

- Artificial compliance introduced by intrinsic cohesive zone models is presented and discussed thoroughly by simulating a simple one-dimensional problem and mixed-mode SE(B) test.
- Motivation for the use of a bilinear CZM is presented in the context of the prediction of fracture in asphalt concrete.
- Time and temperature effects in bulk materials are taken into account to explore viscoelastic fracture behavior of asphalt concrete.
- Mixed-mode SE(B) viscoelastic simulation, in which cohesive elements with a regular pattern are inserted over an area in absence of known crack paths, is performed successfully and the predicted crack trajectory is found to match well with that of experiments.
- A detailed discussion of numerical convergence in the context of mesh discretization and nonlinear equation solvers is presented.

## Acknowledgements

We are grateful to the support from the SemMaterials Company and the National Science Foundation (NSF) through the GOALI project CMS 0219566 (Program Manager, P.N. Balaguru). We also thank anonymous reviewers for their insightful remarks which contributed to improve the manuscript. Any opinions expressed herein are those of the writers and do not necessarily reflect the views of the sponsors.

## References

[1] Barenblatt GI. The formation of equilibrium cracks during brittle fracture: general ideas and hypothesis, axially symmetric cracks. Appl Math Mech (PMM) 1959;23:622–36.
[2] Barenblatt GI. Mathematical theory of equilibrium cracks in brittle fracture. Adv Appl Mech 1962;7:55–129.
[3] Dugdale D. Yielding of steel sheets containing slits. J Mech Phys Solids 1960;8:100–4.

[4] Needleman A. A continuum model for void nucleation by inclusion debonding. ASME J Appl Mech 1987;54:525–31.
[5] Xu X-P, Needleman A. Numerical simulations of fast crack growth in brittle solids. J Mech Phys Solids 1994;42(9):1397–434.
[6] Camacho GT, Ortiz M. Computational modeling of impact damage in brittle materials. Int J Solids Struct 1996;33:2899–938.
[7] Geubelle PH, Baylor JS. Impact-induced delamination of composites: a 2D simulation. Compos Part B 1998;29B:589–602.
[8] Espinosa HD, Zavattieri PD. A grain level model for the study of failure initiation and evolution in polycrystalline brittle materials. Part I: Theory and numerical implementation. Mech Mater 2003;35:333–64.
[9] Knauss WG. On the steady propagation of a crack in a viscoelastic sheet: experiments and analysis. In: Kausch HH, Jaffee R, editors. Deformation and fracture of high polymers. New York: Plenum Press; 1973. p. 501–41.
[10] Schapery RA. A theory of crack initiation and growth in viscoelastic media. Int J Fracture 1975;11:141–59.
[11] Knauss WG, Losi GU. Crack propagation in a nonlinearly viscoelastic solid with relevance to adhesive bond failure. ASME J Appl Mech 1993;60:793–801.
[12] Rahul-Kumar P, Jagota A, Bennison SJ, Saigal S, Muralidhar S. Polymer interfacial fracture simulations using cohesive elements. Acta Mater 1999;47(15):4161–9.
[13] Allen DH, Searcy CR. A micromechanical model for a viscoelastic cohesive zone. Int J Fracture 2001;107:159–76.
[14] Bazant ZP, Li Y-N. Cohesive crack model with rate-dependent opening and viscoelasticity: I. Mathematical model and scaling. Int J Fracture 1997;86:247–65.
[15] Xu C, Siegmund T, Ramani K. Rate-dependent crack growth in adhesives I. Modeling approach. Int J Adhes Adhes 2003;23:9–13.
[16] Majidzadeh K, Kauffmann EM, Ramsamooj DV. Application of fracture mechanics in the analysis of pavement fatigue. Proc Assoc Asphalt Paving Technol 1971;40:227–46.
[17] Abdulshafi AA, Majidzadeh K. J-integral and cyclic plasticity approach to fatigue and fracture of asphalt mixes. Transport Res Rec 1985;1034:112–23.
[18] Kim KW, El Hussein HM. Effect of differential thermal contraction on fracture properties of asphalt materials at low temperature. Proc Assoc Asphalt Paving Technol 1995;64:474–99.
[19] Bhurke AS, Shih EE, Drzal LT. Fracture morphology and fracture toughness measurement of polymer-modified asphalt concrete. Transport Res Rec 1997;1590:23–33.
[20] Soares JB, Colares de Freitas FA, Allen DH. Crack modeling of asphaltic mixtures considering heterogeneity of the material. Washington DC: Transportation Research Board (CD-ROM); 2003.
[21] Tvergaard V. Effect of fiber debonding in a whisker-reinforced metal. Mater Sci Engng 1990;125:203–13.
[22] Paulino GH, Song SH, Buttlar WG. Cohesive zone modeling of fracture in asphalt concrete. In: Petite C, Al-Qadi I, Millien A, editors. Proceedings of the fifth RILEM international conference on cracking in pavements: mitigation, risk assessment and prevention, Limoges, France, 2004. p. 63–70.
[23] Song SH, Paulino GH, Buttlar WG. Simulation of crack propagation in asphalt concrete using an intrinsic cohesive zone model. ASCE J Engng Mech, in press.
[24] Song SH, Paulino GH, Buttlar WG. Simulation of mode I and mixed-mode crack propagation in asphalt concrete using a bilinear cohesive zone model. Washington D.C.: Transportation Research Board (CD-ROM); 2005.
[25] ABAQUS user's manual-version 6.5. Hibitt, Karlsson and Sorenson, Pawtucket, R.I. 2005.
[26] Song SH. Fracture of asphalt concrete: a cohesive zone modeling approach considering viscoelastic effects. Ph.D. Thesis, Department of Civil and Environmental Engineering, University of Illinois at Urbana-Champaign, 2006.
[27] Klein PA, Foulk JW, Chen EP, Wimmer SA, Gao, H. Physics-based modeling of brittle fracture: cohesive formulations and the applications of meshfree methods. SAND 2001-8009. 2001.
[28] Tschoegl NW. The phenomenological theory of linear viscoelastic behavior: an introduction. Germany: Springer-Verlag; 1989.
[29] Christensen RM. Theory of viscoelasticity. New York: Dover Publications, Inc.; 2003.
[30] Rahulkumar P, Jagota A, Bennison SJ, Saigal S. Cohesive element modeling of viscoelastic fracture: application to peel testing of polymers. Int J Solids Struct 2000;37:1873–97.
[31] Park SW, Kim YR. Interconversion between relaxation modulus and creep compliance for viscoelastic solids. J Mater Civil Engng 1999;11(1):76–82.
[32] Hiltunen DR, Roque R. The use of time-temperature superposition to fundamentally characterize asphaltic concrete mixtures at low temperatures. In: Gerald A, Dale S, editors. Engineering properties of asphalt mixtures and the relationship to performance. ASTM STP 1265. Philadelphia: American Society for Testing and Materials; 1994.
[33] AASHTO T322-03. Standard test method for determining the creep compliance and strength of hot mix asphalt (HMA) using the indirect tensile test device. In: Standard specifications for transportation materials and methods of sampling and testing, 24th edition. 2004.
[34] Buttlar WG, Roque R. Development and evaluation of the new SHRP measurement and analysis system for indirect tensile testing of asphalt mixtures at low temperatures. Transport Res Rec 1994;1454:163–71.
[35] Wagoner MP, personal communication, 2005.
[36] Wagoner MP, Buttlar WG, Paulino GH. Disk-shaped compact tension test for asphalt concrete fracture. Exp Mech 2005;45:270–7.
[37] Wagoner MP, Buttlar WG, Paulino GH, Blankenship P. Investigation of the fracture resistance of hot-mix asphalt concrete using a disk-shaped compact tension test. Transport Res Rec 2005;1929:183–92.
[38] Shah SP, Swartz SE, Ouyang C. Fracture mechanics of concrete: applications of fracture mechanics to concrete, rock, and other quasi-brittle materials. New York: John Wiley and Sons; 1995.
[39] Roy YA, Dodds Jr RH. Simulation of ductile crack growth in thin aluminum panels using 3-D surface cohesive elements. Int J Fracture 2001;110:21–45.

[40] Han T-S, Ural A, Chen C-H, Zehnder AT, Ingraffea AR, Billington SL. Delamination buckling and propagation analysis of honeycomb panels using a cohesive element approach. Int J Fracture 2002;115:101–23.
[41] Rots JG, de Borst R. Analysis of concrete fracture in "direct" tension. Int J Solids Struct 1989;25(12):1381–94.
[42] Riks E. An incremental approach to the solution of snapping and buckling problems. Int J Solids Struct 1979;15(7):529–51.
[43] Crisfield MA. A fast incremental/iterative solution procedure that handles "snap-through". Comput Struct 1981;13:55–62.
[44] Powell G, Simons J. Improved iterative strategy for nonlinear structures. Int J Numer Meth Engng 1981;17:1455–67.
[45] Kim J-H. Mixed-mode crack propagation in functionally graded materials. Ph.D. Thesis, Department of Civil and Environmental Engineering, University of Illinois at Urbana – Champaign. 2003.